Bulletin of Engineering Geology and the Environment (2024) 83:386
https://doi.org/10.1007/s10064-024-03888-3

ORIGINAL PAPER

Mining-induced fault failure and coseismic slip based on numerical investigation

Yatao Li[1] · Eiichi Fukuyama[1] · Nana Yoshimitsu[1]

Received: 27 July 2023 / Accepted: 28 August 2024

Abstract

Assessing the risk of mining-induced earthquakes is crucial for mining safety and disaster mitigation. In this study, we investigated fault failure and coseismic slip as mining activities approach the fault, using a 2-D plane strain model. We focused on the stress ratio of shear stress to normal stress on the fault (k) and coseismic slip on the fault in relation to variables such as the working face location, fault dip angle, fault friction coefficient (μ_s), and depth-dependent background stress field. We examined two models, one with infinite μ_s (i.e. no fault failure) to analyze total stress disturbance on the fault, and another with finite μ_s ranging between 0.5 and 0.8 to estimate coseismic slip. Our study yields the following key findings. Fault reactivation induced by mining activities is primarily caused by an increase in k rather than by an increase in shear stress. Hanging wall mining induces instability beneath the mining level, whereas footwall mining provokes instability above it. By utilizing the concept of the fault stress ratio (k), this study elucidates the mechanisms responsible for the pronounced instability induced by footwall mining. Fault stability is highly sensitive to the fault dip angle and mining distance, which are crucial factors in assessing the potential for induced earthquakes. Higher μ_s values lead to small regions of coseismic slip under the same stress environment. Based on these findings, we interpreted a possible cause of the induced earthquake at the Yuejin coal mine on August 11th, 2010, and introduced a quantitative approach for establishing the terminal mining line.

Keywords Mining-induced earthquakes · Fault stress ratio · Fault failure · Coseismic slip · Terminal mining line

Introduction

Since the advent of deep mining operations worldwide, mining-induced earthquakes have emerged as a significant concern due to their potential to cause severe damage to mining infrastructure and surrounding areas (Mark 2016; Wei et al. 2018; Kang et al. 2023). Verdon et al. (2018) conducted a comprehensive investigation on an earthquake associated with longwall mining operations at Thoresby Colliery, Nottinghamshire, one of the deep coal mines in the United Kingdom. They presented compelling evidence that the mining operations directly induced seismic events in the region. The reactivation of faults due to mining operations can occasionally lead to catastrophic rock (coal) and gas outbursts (Cao et al. 2001; Karacan et al. 2008; Balsamo et al. 2010). For example, a coal burst accident in the Yima Qianqiu coal mine in China in November 2011 was attributed to fault reactivation (Cai et al. 2021). At the No. 25,110 working face of the Yuejin coal mine in China, a total of 20 coal burst accidents were caused by fault reactivation as mining activities gradually approached the F16 fault (Li et al. 2014).

Given the increasing demand for coal resources and the ongoing trend of mining at greater depths, the risk associated with mining-induced earthquakes could potentially escalate in the forthcoming years (Ranjith et al. 2017). Currently, coal mining operations in China extend to increasingly greater depths at 8–25 m annually. By the end of 2022, more than 50 coal mines in China had reached mining depths of over 1000 m, with the deepest mine reaching a depth of 1510 m (Kang et al. 2023). Deep mining operations in proximity to faults can prompt sudden failure of coal and adjacent rocks, culminating in roadway roof collapse due to

✉ Yatao Li
li.yatao.36k@st.kyoto-u.ac.jp

[1] Department of Civil and Earth Resources Engineering, Kyoto University, Kyoto, Japan

Published online: 07 September 2024

violent strain energy release (Chen et al. 2018; Wang et al. 2021; Li et al. 2007; Foulger et al. 2018; Zhou et al. 2022).

Theoretically, stress disturbance due to faulting is rigorously expressed by the slip distribution on the fault as representation theorem (e.g., Aki and Richards 2002; Kostrov and Das 1988). To properly incorporate the effect of the stress field on the fault, friction theory (e.g., Jaeger et al. 2007; Scholz 2019) has been employed. Therefore, coseismic fault slip is one of the essential aspects when considering the impact of stress disturbance on fault stability. Given that the faulting caused by deep mining may lead to rock (coal) bursts, considerable research has been conducted to understand the mechanisms underlying mining-induced fault slip (e.g., Wei et al. 2020). Song and Liang (2021) employed numerical simulation methods to investigate the impact of hanging wall mining. They studied the mechanism behind groundwater outbursts resulting from fault activity, with a particular focus on the perspective of induced stress concentration. Wu et al. (2021) analyzed the behavior of a working face as it advanced towards the hanging wall of a normal fault, focusing on investigating the influence of different coal pillar widths from the abutment pressure and found that high dip faults were more likely to induce earthquakes. Shan et al. (2023) investigated the characteristics of excavation-induced pressure unloading and fault slip in the overlying rock mass during mining parallel to the fault using the finite difference method. These studies focused on fault reactivation induced by mining in view of the stress distribution. They carefully considered increased abutment pressure, stress concentration, and pressure unloading, attributing the stress change due to mining as a primary cause of fault instability.

Past studies on fault instability caused by mining activities primarily focused on shear stress concentration and did not discuss the changes in normal stress (Wei et al. 2020; Song and Liang 2021; Shan et al. 2023; Wu et al. 2021; Jiao et al. 2021; Lyu et al. 2021; Zhang et al. 2023; Zhu et al. 2021). In contrast, we introduce an approach based on the Mohr-Coulomb criterion as our rock failure criterion, emphasizing the critical role of normal stress in fault instability. We consider the fault stress ratio, which is defined as the ratio of shear stress to normal stress on the fault. It provides a more accurate measure of fault stability. This stress ratio is crucial, as mining activities induce perturbations both in shear and normal stress on the fault. Therefore, it is essential to take into account both shear and normal stress in assessing mining-induced earthquakes. In our research, we systematically investigated mining-induced fault instability by employing the fault stress ratio.

In our approach, we consider two aspects of fault reactivation: fault failure and coseismic slip. The magnitude of induced earthquake events is primarily influenced by the extent of coseismic slip rather than just stress, highlighting the necessity of in-depth investigations into both fault failure and coseismic slip processes. To achieve this, we utilize two models. The first model investigates mining-induced stress disturbances and the fault stress ratio using a model with infinite fault frictional strength. The second model introduces a friction coefficient on the fault, allowing us to quantitatively study coseismic slip distribution concerning various factors such as mining distance and background stress ratio. These two models provide a better understanding of the mechanisms behind mining-induced fault instability.

Moreover, our study addresses a gap in existing research by questioning the applicability of traditional terminal mining line designs in deep mining operations under high tectonic stress environments near faults. By investigating the mining-induced fault stress ratio and coseismic slip along the fault, our analysis offers insights into the underlying mechanisms of mining-induced fault instability. In this study, we constructed a fault reactivation model tailored to the conditions at the Yuejin coal mine in China, specifically investigating the impacts of fault failure and coseismic slip as the mining face approaches the fault.

Numerical modeling procedures

Model overview and input parameters

We utilized a 2-D plane-strain model employing a thin rectangular volume, as depicted in Fig. 1. The computational volume measured 2400 m in length along the mining direction (x-direction), 1200 m in the vertical direction (z-direction) and had a width of 10 m (y-direction). Since the origin was situated at the left bottom corner of the modeling region and the positive direction was defined as upward. The depth, denoted as h, was expressed as $h = 1600 - z$. In this model, the depth ranged from 400 m to 1600 m. The key governing equation used in static equilibrium analysis was written as follows;

$$\nabla \cdot \boldsymbol{\sigma} + \boldsymbol{F} = 0 \tag{1}$$

where $\boldsymbol{\sigma}$ is the total stress tensor, and $\boldsymbol{F}$ represents the body forces, including gravity. We introduced the following displacement boundary conditions,

$$\begin{aligned} u_x &= 0 \quad \text{at } x = 0 \text{ m} \\ u_y &= 0 \quad \text{at } y = m \quad \text{and } y = 10 \text{ m}, \quad \text{and} \\ u_z &= 0 \quad \text{at } h = 1600 \text{ m} \end{aligned} \tag{2}$$

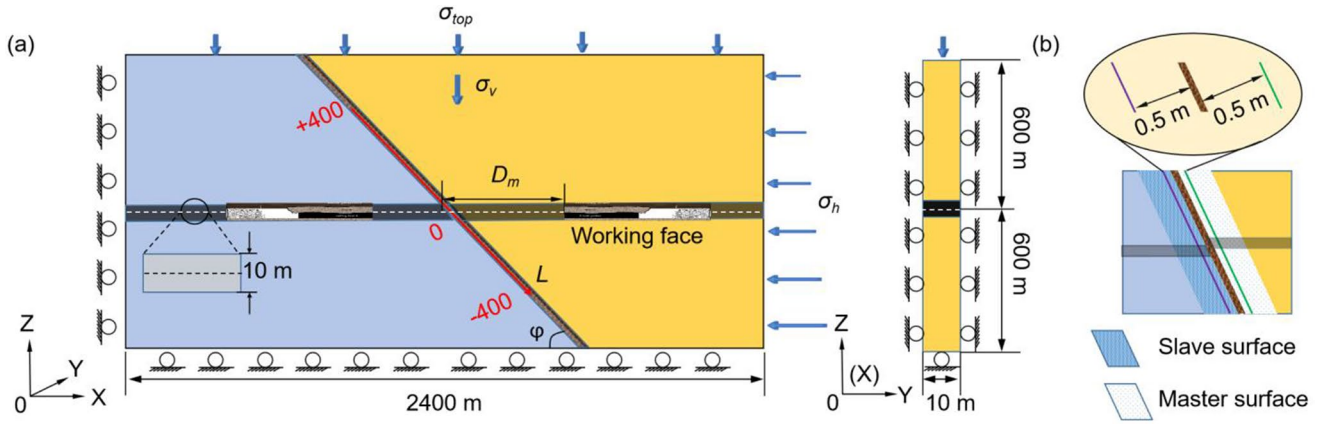

Fig. 1 A schematic illustration of the 2-D plane strain model, including the coal mining working face and the fault ahead of the working face. **a** The *xyz*-coordinate system is set as shown in the bottom left of the figure. The origin is located at the bottom left corner of the modeling region. σ_{top} is the σ_{zz} stress at the top of the model that simulates overburden weight. σ_v is vertical principal stress. σ_h is horizontal principal stress in the *x*-direction. On the left and bottom sides of the model, the displacement boundary condition is applied as described in the text. φ stands for fault dip angle. The local coordinate (red line) L is set along the fault, being the origin is at the center of the coal seam, and the positive direction of L is taken upward. D_m is the mining distance measured from the origin of the local coordinate L to the working face, taken positive at the hanging wall side. The thickness of the coal seam is 10 m. **b** Master and slave surfaces are applied to the model. The green line, located 0.5 m from the fault, represents the measurement line, along which τ, σ_n, and coseismic slip are measured on the hanging wall side. Similarly, the purple line, positioned 0.5 m away from the fault, represents the measurement line on the footwall side

where u_i is *i*-component displacement, and i takes either x, y, or z.

Next, we set the following stress boundary conditions,

$$\begin{aligned} \sigma_v &= \rho g h \\ \sigma_h &= r_b \sigma_v \end{aligned} \tag{3}$$

where σ_v and σ_h are vertical and horizontal far field principal stress, ρ is the density, and g is the gravitational acceleration. Compression stress was assigned positive in this study. r_b was the background stress ratio defined as

$$r_b = \frac{\sigma_h}{\sigma_v} \tag{4}$$

We defined the fault stress ratio k as

$$k = \frac{\tau}{\sigma_n} \tag{5}$$

where τ is shear stress, and σ_n is normal stress on the fault. It should be noted that k controls the fault stability. We used the Mohr-Coulomb criterion to evaluate the fault failure, as shown in Eq. (6)

$$\tau_f = C + \mu_s \sigma_n \tag{6}$$

where τ_f is the fault frictional strength, σ_n is the normal stress applied on the fault, μ_s is the friction coefficient, and C, the cohesion is assumed to be zero. By comparing k with μ_s (orτ *with* τ_f), we could evaluate the stability of the reverse fault due to mining-induced stress disturbance and coseismic slip.

We investigated the effect of parameters such as r_b, fault dip angle φ, and mining distance D_m on k. It should be noted that D_m represented the distance between the fault and the mining face, and was considered positive when the mining face was located on the hanging wall side. In this study, we considered two background stress ratios, $r_b = 2$ and 3, six φ at every 10° from 20° to 70°, and D_m ranging between 0 m and 200 m, with a constant panel width of 200 m. We assumed that coal seam and rock layers have the same density and elastic properties in the computation area, as shown in Table 1. In order to calculate the distribution of total stress change on the fault under the mining activities, we assumed that the fault frictional strength was infinite (i.e., μ_s

Table 1 Parameters of the numerical model

Parameters	Values	Parameters	Values
Young's modulus, E (GPa)	15	Cohesion stress, C (MPa)	0
Poisson's ratio, v	0.25	Depth, h (m)	400–1600
Shear modulus, G (GPa)	6.5	Mining distance, D_m (m)	-200-200
Density, ρ (kg/m^3)	2400	Mining level, (m)	1000
Fault dip angle, φ (°)	20–70 (30)*	Panel width, (m)	200
Background stress ratio, r_b	2 or 3 (1.5)*	Mining thickness, (m)	10 (11.5)*
Friction coefficient, μ_s	0.5–0.8	Dip angle of the coal seam, (°)	0 (12)*

* The parameters in brackets represent the actual parameters of the Yuejin coal mine from Cai et al. (2021)

is infinite, and no slip is allowed to occur) and measured the stress disturbance on the fault. Subsequently, we computed k by introducing the Mohr-Coulomb criterion with various μ_s.

As shown in Fig. 1, we introduced a local coordinate denoted as L along the fault. The origin of L was set at the intersection of the fault and the center of the coal seam layer, taking upward as positive and downward as negative. Using L facilitated the understanding of the spatial relationship between k, D_m, and φ.

The characteristic feature of k as a function of r_b and φ

Before conducting the simulation, a theoretical analysis was performed to investigate the characteristic feature of k as a function of r_b and φ within a reverse fault environment by adjusting the background stress to the local coordinate system. These theoretical solutions enabled us to gain basic insights into how much r_b and φ affected k distribution on the fault. In Fig. 2a, it was observed that as r_b increases, k also increases. Figure 2b shows the critical angle represented by the marked stars. When r_b was held constant, and φ was smaller than the critical angle, increasing φ led to an increase in k. Conversely, when φ was larger than the critical angle, increasing φ resulted in a decrease in k. Furthermore, the analysis conducted in Fig. 2 revealed that under the same background stress, a smaller φ resulted in a larger magnitude of k, potentially increasing the risk of mining-induced earthquakes.

Numerical simulation and mesh generation

We used the finite element method software Code_Aster (Ver. 14.6) to simulate the coal mining-induced faulting process (see http://www.code-aster.org for details). The mining-induced stress disturbance and coseismic slip on the fault were calculated using a 2-D plane strain model, as shown in Fig. 1. Salome-Meca Ver. 2015.1 was utilized as the pre-and post-processor for Code_Aster, to construct a mesh model consisting of 216,486 tetrahedron elements with nodes set on the vertex. The dimensions of the elements were kept smaller than 10 m. On the contacting interfaces between the upper and the lower fault surfaces, the dimension of the elements was set to less than 1 m using the sub-mesh method, as shown in Fig. 1b.

Analysis of mining-induced fault failure and coseismic slip

Investigation of stress perturbations and k-disturbance along fault

Characterization of mining-induced stress distribution along fault

In our analysis, we measured the stress disturbance resulting from mining activities by assuming that the fault shear strength was infinite. Subsequently, we evaluated the influence of mining-induced stress distribution along the fault as a function of D_m.

Figure 3 illustrates the stress distribution along the fault in the specific case of D_m = 20 m, r_b = 3, and φ=20º. In

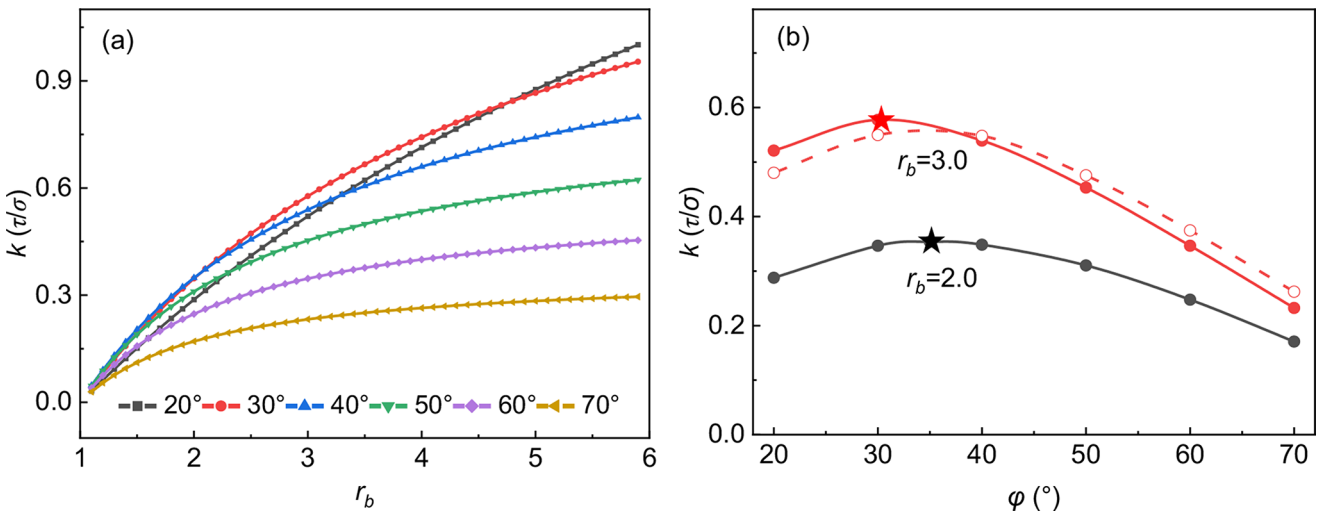

Fig. 2 Distribution of k as a function of r_b and φ. **a** Distributions of k, as a function of r_b when φ is 20°, 30°, 40°, 50°, 60°, and 70°. **b** Distributions of k as a function of φ for the cases where r_b = 2 and 3. Red and black stars represent the maximum value of k (k_{max}). The dashed line with open circles represents the distributions of k at L=200 m (Fig. 5a), as a function of φ

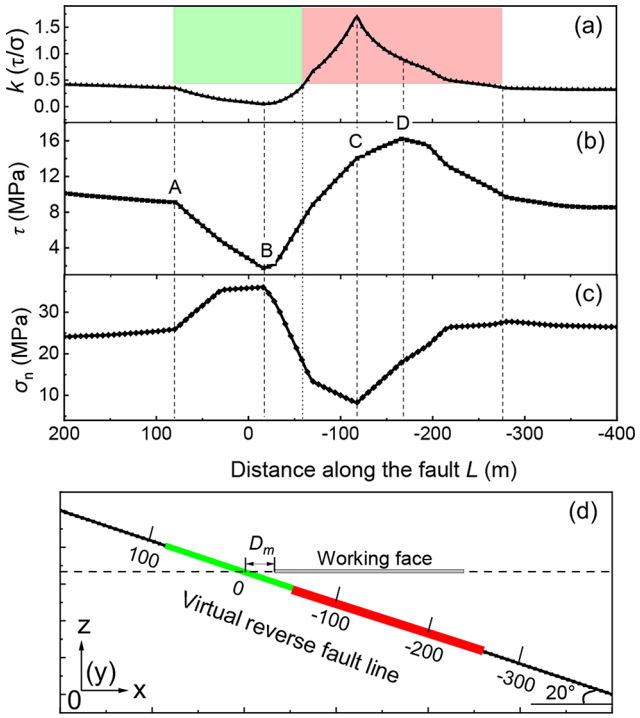

Fig. 3 Mining-induced stress distribution along the fault when D_m = 20 m, r_b = 3, and φ = 20°. **a** distribution of k, **b** distribution of τ, and **c** distribution of σ_n along the fault. **d** The geometry between the fault (black, green, and red lines) and the working face (gray solid horizontal line). Green and red areas/lines in **a** and **d** stand for where k decreases and increases due to mining activity, respectively

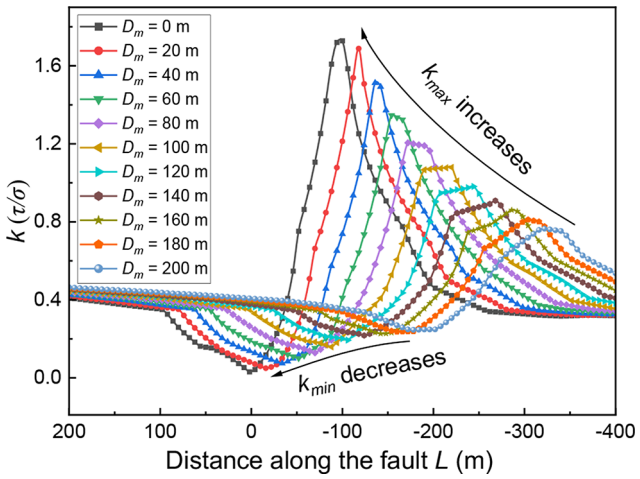

Fig. 4 The distribution of k along the fault as a function of distance along the fault. Different color corresponds to different D_m when r_b = 3 and φ = 20°

Fig. 3b, the shear stress τ at point A (L = 80 m, L stands for the coordinate along the fault dip) on the fault was 9.1 MPa. As we moved along point B (L = -18 m), the stress gradually decreased to a minimum value of 1.7 MPa. Then, it increased to the maximum value of 16.2 MPa at point D (L = -168 m). At depths deeper than point D (L = -168 m), τ decreased again and reached a constant value of 8.7 MPa around L = -350 m. The normal stress (σ_n) shown in Fig. 3c exhibits an opposite behavior. It began to vary from 25.9 MPa at point A (L = 80 m), increased to its highest value of 36 MPa at point B (L = -18 m), then decreased to 8.3 MPa at point C (L = -118 m), and increased again to L = -220 m achieving the constant value of 26.4 MPa.

Examining the stress ratio k, as shown in Fig. 4a, it was found to vary from 0.35 at point A (L = 80 m) to a minimum value of 0.05 at point B (L = -18 m). Subsequently, k increased to a maximum of 1.69 at point C (L = -118 m), then decreased again until reaching a constant value of 0.32 at L = -350 m along the fault. In the area above point A (L = 80 m) on the fault, k was a constant value of 0.35. Since τ and σ_n were constant in this region, the mining effect was considered negligible.

Based on the above results, we could observe that τ and σ_n decreased along the fault above L = -60 m. Since the mining-induced τ decreased faster than σ_n, this resulted in a decrease in k and an increase in fault stability. On the other hand, for the case below L = -60 m, an increase in k could make the fault unstable and generate a coseismic slip. Therefore, the term fault stress ratio k could be used to quantify fault stability. It is insightful to perform a fault instability analysis prior to the fault with finite strength.

The relationship between D_m and k

To assess the risk of mining-induced fault reactivation, we analyzed the dependence of k on D_m. Figure 4 depicts the variation of k as the mining activity approached the fault when r_b = 3 and φ = 20°. It could be observed that the maximum value of k (k_{max}) increased when the working face gradually approached the fault. For example, when D_m = 100 m, the maximal value k_{max} became 1.1 at L = -220 m, then gradually increased to 1.7 at L = -100 m when D_m = 0 m. Simultaneously, the minimum value of k (k_{min}) decreased gradually as mining activity approached the fault.

In Fig. 4, k_{min} was proportional to D_m, which indicates that the mining activity contributed to stabilizing the fault. In contrast, the increase in k_{max} as D_m decreases indicated that mining activity had the potential to make the fault unstable in this specific area. The value of D_m, determined based on the findings of this study, was crucial in evaluating fault instabilities and mitigating the risk of induced earthquakes.

The influence of φ on the distribution of k

We investigated the effect of φ on the distribution of k by altering φ at every 10° interval from 20° to 70° and show the results in Fig. 5. The investigation was performed under

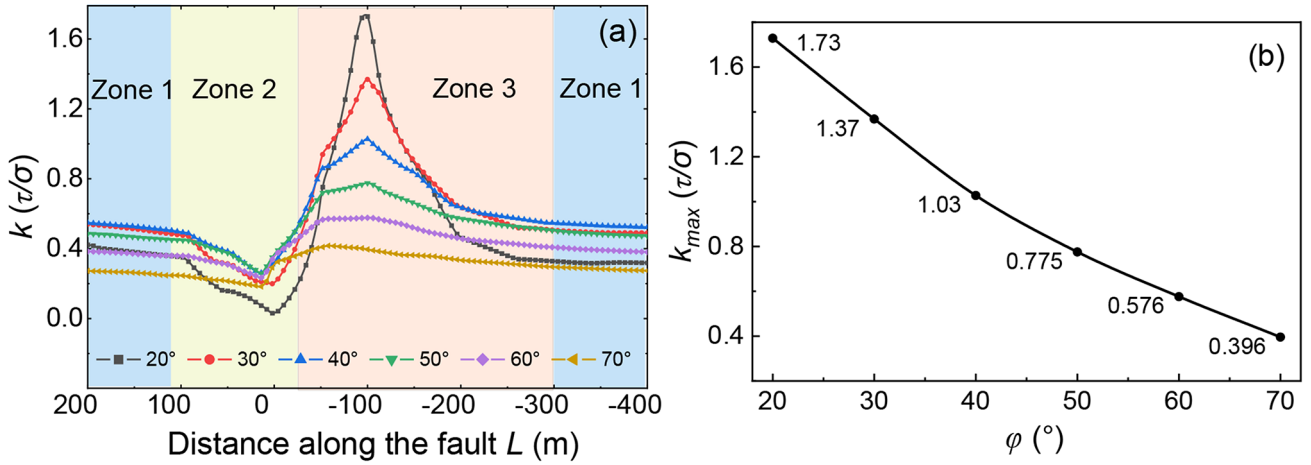

Fig. 5 Distribution of k along the fault with different φ when $D_m = 0$ m and $r_b = 3$. **a** Distribution of k for φ from 20° to 70° at 10° intervals. Zone 1 represents the initial area where no mining-induced stress disturbances occur. Zone 2 corresponds to an area where mining activities lead to an increase in fault stability. In contrast, Zone 3 denotes an area where mining operations result in a decrease in fault stability; **b** Variation of k_{max} as a function of φ at L = -100 m

$r_b = 3$ and $D_m = 0$ m. The results showed that the value of k remains constant from $L = 100$ m to $L = 200$ m along the fault. This implied that the mining activities do not have a significant impact on the value of k. Therefore, we evaluated the k values at $L = 200$ m as the mining-unaffected ones and plotted the result in Fig. 2b. Notice that the curve with open circles in Fig. 2b indicated the dependence of k as a function of fault dip angle φ. It slightly increased at $20° \leq \varphi \leq 30°$ and decreased at $40° \leq \varphi \leq 70°$. From the plots shown in Fig. 2b, it was concluded that the numerical results were validated by the theoretical ones explained in Sect. 2.2.

In Fig. 5, we observed that φ significantly affects the distribution of k along the fault. Specifically, from the results shown in Fig. 5a, for different values of fault dip angle φ, the corresponding range of k values could be determined. For example, when $\varphi = 70°$, k ranged from 0.18 to 0.40; in the case of $\varphi = 40°$, k ranged from 0.26 to 1.03; and for $\varphi = 20°$, k ranged from 0.03 to 1.73. Thus, we found that a smaller value in φ induces a larger value in k. Figure 5a showed that k along the fault was sensitive to φ. Therefore, the coal mining activities in the vicinity of a fault with a small φ could cause drastic k changes and have a larger potential to induce earthquakes. Figure 5c shows the variation of k_{max} as a function of φ. k decreased gradually from 1.73 to 0.4 as φ increased from 20° to 70°. The above results suggested that φ significantly influenced the range of k and its distribution along the fault.

In Fig. 5a, the mining site could be divided into three distinct zones. In Zone 1, the initial area demonstrated stability without significant changes. Zone 2, on the other hand, experienced an increase in fault stability due to mining-induced k decrease. Conversely, mining operations in Zone 3 resulted in a decrease in fault stability.

Coseismic fault slip under contact friction

σ_n, τ, k, and coseismic slip distribution

After analyzing the stress distribution using the infinite μ_s fault model, further investigation was conducted using the finite μ_s model by introducing contact interfaces on the fault. Specifically, we evaluated the stress drop under the conditions of $r_b = 2$ and $\varphi = 30°$. The stress drop was measured as the difference in τ between the hanging wall and the footwall sides. In this study, we introduced a new term called 'k-drop' (Δk), which is defined as the difference between k on the hanging wall side ($k_h = \tau^h/\sigma_n^h$) and that on the footwall side ($k_f = \tau^f/\sigma_n^f$).

$$\Delta k = k_h - k_f \tag{7}$$

where τ^h, σ_n^h, τ^f and σ_n^f represent the shear and normal stress on the hanging wall and footwall sides of the fault, respectively. These stresses were evaluated at the locations 0.5 m off the fault, as indicated in Fig. 1b, as purple and green thin lines, respectively. In the third panel of Fig. 6a, k also generated some difference as the stress drop induced Δk as observed in Figs. 6b and c. It should be emphasized that this definition for Δk is only valid for reverse fault environments.

Figure 6 shows the distributions of σ_n, τ, k, and coseismic slip along the fault, assuming that $\mu_s = 0.55$ and $D_m = 90$ m. In Fig. 6b and c, we could observe that τ decreased and generated a stress drop where k was larger than 0.55 due to mining activity. This indicates that the regions with larger values of k were more prone to experiencing stress drop due to coseismic slip on the fault. In contrast, σ_n remained relatively unchanged above and below the fault. The coseismic

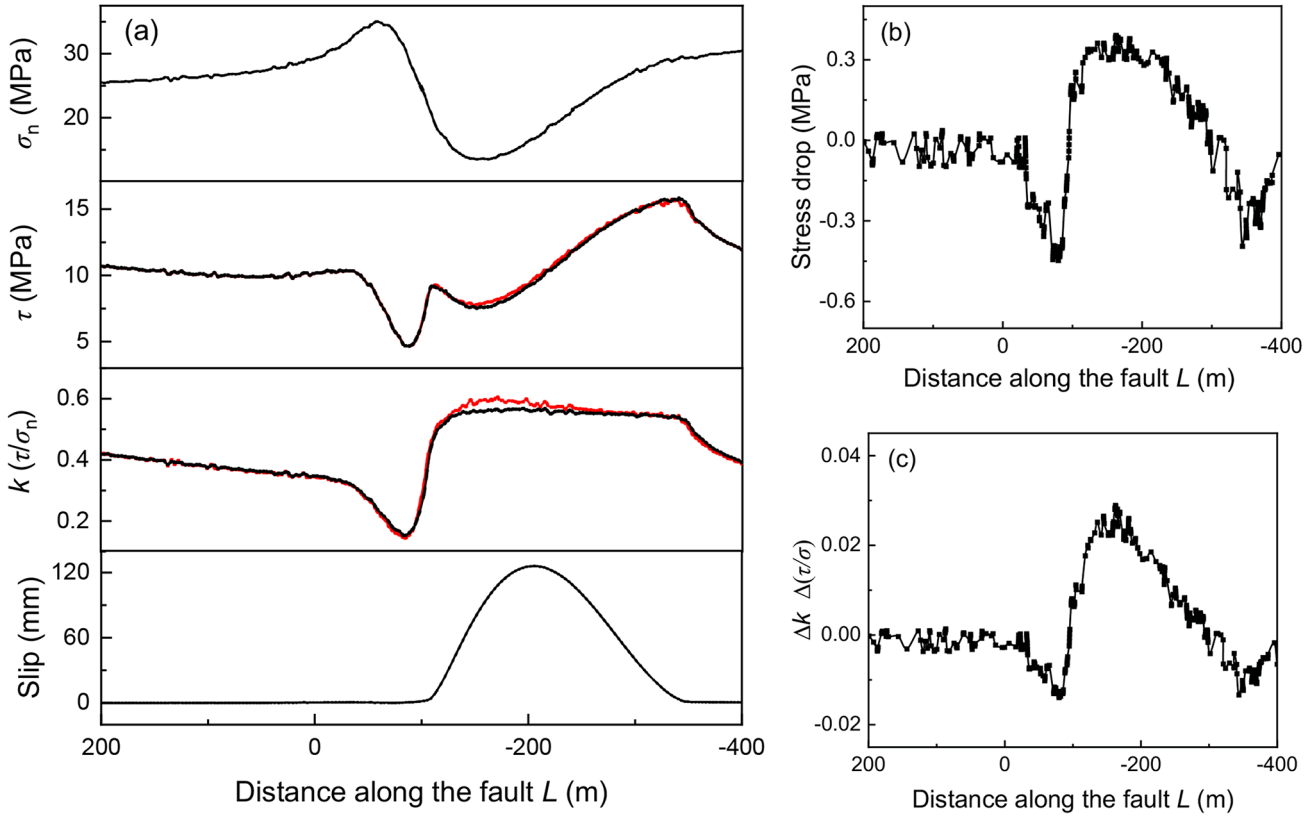

Fig. 6 Distributions of σ_n, τ, k, and coseismic slip along the fault under the condition of $D_m = 90$ m, $\mu_s = 0.55$, and $\varphi = 30°$. **a** Distributions of σ_n, τ, and k on the hanging wall and footwall, respectively. The red curves represent τ and k at the hanging wall side, and the black curves represent τ and k at the footwall side. The bottom trace is the distribution of coseismic slip on the fault. **b** Stress drop distribution in τ of Fig. 6a. **c** Δk distribution in k of Fig. 6a

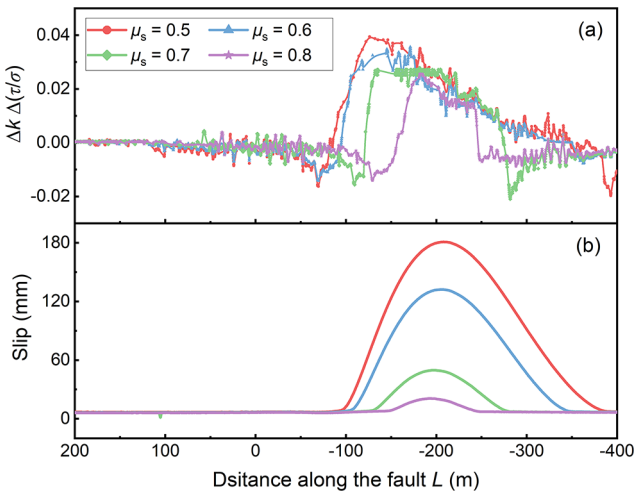

Fig. 7 Distribution of **a** Δk and **b** coseismic slip along the fault for different μ_s from 0.5 to 0.8 under the condition of $r_b = 2$, $D_m = 90$ m, and $\varphi = 30°$

slip occurred in the region where k exceeded the threshold condition of $\mu_s = 0.55$. The slip zone was confined to the region below the mining level, specifically, ranging from L = -110 m to -340 m along the fault. The largest slip (0.14 m) was observed at L = -200 m on the fault. Note that the slip was asymmetric concerning L = -200 m along the fault. Therefore, an asymmetrical slip could be attributed to the asymmetric distribution for L = -200 m of the Δk along the fault. The asymmetric slip distribution disappeared if φ was close to 90°. Figures 6b and c reveal that Δk and stress drop exhibit different shapes, attributed to the influence of σ_n (as shown in the top panel of Fig. 6a) with varying values across different positions within the slip zone.

Δk distribution for various μ_s

To investigate the influence of μ_s on the distribution of Δk along the fault, we varied the value of μ_s from 0.5 to 0.8. As shown in Fig. 7, the length of Δk region decreased from 296 m (from L = -89 m to L = -385 m) for $\mu_s = 0.5$ to 98 m (from L = -152 m to L = -250 m) for $\mu_s = 0.8$. In contrast, as μ_s decreased from 0.8 to 0.5, it was observed that the coseismic slip zone increased from 90 m to 280 m, respectively. Our analysis revealed that higher values of fault frictional strength (μ_s) result in larger Δk occurrences due to nearby mining activities. In contrast, lower values of μ_s

Table 2 Fault coseismic slip for different μ_s (D_m = 90 m)

μ_s	Maximum slip (mm)	Slip zone length (m)
0.5	180	280
0.6	130	230
0.7	50	148
0.8	20	90

were associated with expanded coseismic slip zones. The data presented in Table 2 provided a summary of coseismic slip instances characterized by distinct μ_s.

Influence of D_m on coseismic slip in hanging wall and footwall mining

Figure 8a illustrates the coseismic slip distribution above the mining level on the fault, considering the variation of D_m from − 10 m to -170 m at 40 m intervals with $r_b = 2$ and $\mu_s = 0.7$. The fault began to slip at slightly larger than D_m = -200 m. With the working face approaching the fault from D_m = -170 m to D_m = -10 m, the length of the coseismic slip zone and the maximum slip increased (Table 3).

Figure 8b illustrates the coseismic slip distribution that appeared beneath the mining level on the fault, considering the variation of D_m from 10 m to 170 m at 40 m intervals with r_b = 2 and $\mu_s = 0.7$. The fault began to slip at slightly larger than D_m = 170 m, and with the working face approaching the fault from D_m = -170 m to D_m = -10 m, the length of the coseismic slip zone and the maximum slip increased (Table 3).

Figure 8d presents simulation results based on the actual conditions at the Yuejin coal mine (as depicted in Fig. 8c). These results indicate that the location of the coseismic slip

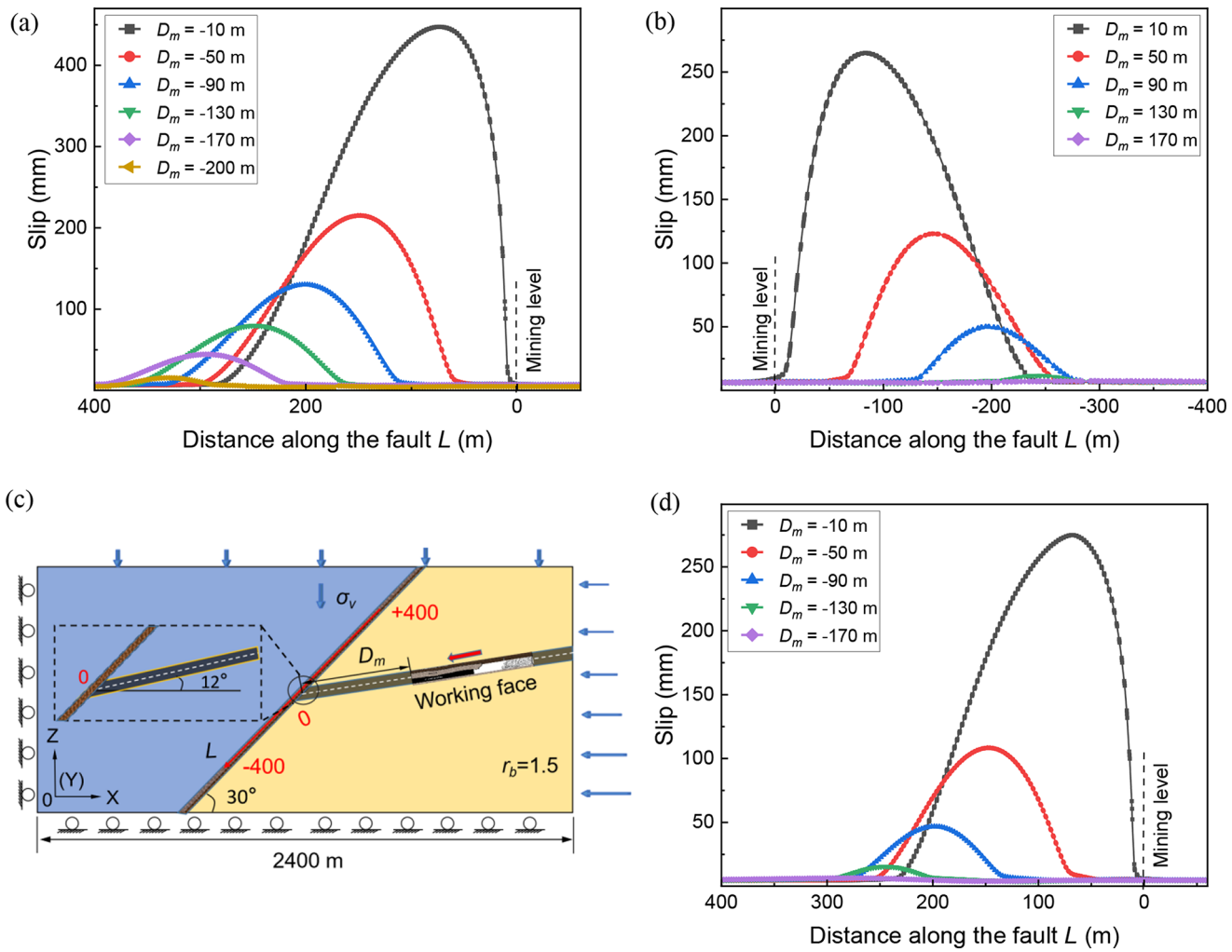

Fig. 8 Slip distributions for different D_m ranging from 10 m to 170 m at 40 m intervals under footwall and hanging wall mining conditions, **a** for footwall mining with $r_b = 2$, $\mu_s = 0.7$, and $\varphi = 30°$, and **b** for hanging wall mining with $r_b = 2$, $\mu_s = 0.7$, and $\varphi = 30°$. **c** A schematic illustration of the 2-D plane strain model based on the conditions at Yuejin coal mine. The scale and coordinate system of the model, including both global and local systems, align with those presented in Fig. 1a. The background stress ratio (r_b) is 1.5. The coal seam, intersected by the fault, lies 1000 m deep, dips at an angle of 12°, and has an average thickness of 11.5 m. **d** Slip distributions with footwall mining at Yuejin coal mine with the conditions r_b = 1.5, $\mu_s = 0.7$, $\varphi = 30°$, and a coal seam dip angle of 12° based on the model shown in **c**

Table 3 Fault coseismic slip for different D_m ($\mu_s = 0.7$)

D_m		Maximum slip (mm)	Slip zone length (m)
Hanging wall mining	10	265	232
	50	123	191
	90	50	138
	130	12	37
	170	7	3
Footwall mining	-10	447	273
	-50	215	240
	-90	130	215
	-130	80	190
	-170	44	159
	-200	14	58
Yuejin coal mine	-10	275	213
	-50	108	178
	-90	46	130
	-130	15	63
	-170	6	3

was situated below the mining level, and the magnitude of this slip, prompted by mining activities, closely parallels the fault slip observed during hanging wall mining (see Fig. 8b; Table 3).

We found that under the same $|D_m|$ conditions, footwall mining resulted in a larger coseismic slip size and dislocation length compared to hanging wall mining, although their relative shape of slip distribution was similar. In other words, footwall mining induced more significant fault instability than hanging wall mining.

Since we assumed depth-dependent background stress, the stress drop differed between the slip zones caused by footwall mining and those caused by hanging wall mining. In contrast, the stress change resulting from mining-induced stress was consistent. Consequently, footwall mining would cause a larger fault slip than hanging wall mining.

Estimation of seismic magnitudes and nucleation size

We estimated the seismic moment, M_0, of the mining-induced earthquake in the case of D_m = 90 m, 50 m, and 10 m. M_0 was defined as follows (Aki 1967; Kanamori and Anderson 1975; Aki and Richards 2009),

$$M_0 = GL_sL_wD \tag{8}$$

where G is the shear modulus of the rocks on the fault, which is 6.5 GPa in this study (Table 1), L_s and L_w are the coseismic slip length and the width along the fault, respectively. D is the average coseismic slip on the fault. Here, we assumed that L_s and L_w followed the empirical relation of $L_s = 2L_w$ for moderate-sized earthquakes (Geller 1976). Therefore, given the conditions that D_m = 90 m, 50 m, and 10 m, L_w was calculated to be 74 m, 87 m, and 115 m, respectively. These calculations also applied to the footwall mining and Yuejin mining conditions, as shown in Table 4. They were consistent with the empirical relationship among M_w, L_s, L_w, and D (Wells and Coppersmith 1994; Wells 2013).

Table 4 Fault parameters and moment magnitudes for the cases computed

D_m (m)		D (mm)	Average L_s (m)	L_w (m)	M_w
Hanging wall mining	10	125	232	116	2.8
	50	55	191	95.5	2.5
	90	24	138	69	2.0
Footwall mining	-10	200	273	136.5	3.1
	-50	102	240	120	2.8
	-90	60	215	107.5	2.6
Yuejin coal mine	-10	130	213	106.5	2.8
	-50	50	178	89	2.4
	-90	20	130	65	2.0

Using M_0 in the unit of Nm, we calculated the moment magnitude M_w from the following equation (Hanks and Kanamori 1979);

$$M_w = \frac{\log M_0 - 9.1}{1.5} \tag{9}$$

The reason why we used moment magnitude (M_w) is that it is based on the physical values. Thus, it is easy and suitable to apply to the present numerical simulation results. When comparing the magnitudes predicted by numerical simulations with those observed in the field, we need to pay attention to the magnitude scale.

The values for M_w were compiled and presented in Table 4. It was crucial to carefully consider the terminal mining lines for deep mining nearby faults, particularly in high tectonic stress environments, to mitigate disastrous fault ruptures. Our simulation results indicated that hanging wall mining generates fault coseismic slip below the mining level when D_m was less than 170 m. As shown in Fig. 9, the length of the coseismic slip zone increased as D_m decreased.

The nucleation length is the critical length of the initial crack where the unstable rupture starts to propagate outward if the initial crack size exceeds the critical size (Uenishi and Rice 2003). The coseismic slip length can be compared with the nucleation length. It is important to highlight that when the slip zone size caused by mining activity exceeds the nucleation zone size, there is a potential to generate a large earthquake by expanding the rupture outside the slip zone. According to Uenishi and Rice (2003), the nucleation length L_n could be expressed under the linear slip weakening law (Andrews 1976) as follows:

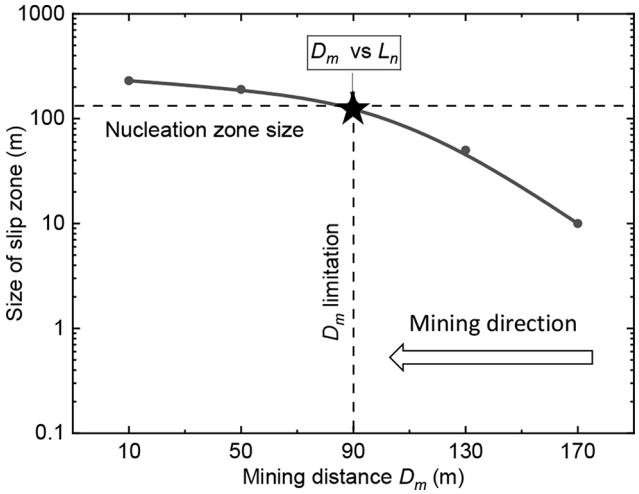

Fig. 9 The relation between the coseismic slip zone size and D_m (see Table 3). The nucleation zone size of 138 m (broken horizontal line) is assumed under the condition that μ_s - μ_d = 0.1, D_c = 0.03 m, and the average normal stress is 20 MPa. The solid star indicates the location of the limit line of D_m

$$L_n = 1.158\frac{ED_c}{2(1-\nu^2)(\tau_f - \tau_d)} \quad (10)$$

where D_c is the slip-weakening distance, E is Young's modulus, ν is Poisson's ratio. τ_f -τ_d is the breakdown strength drop. τ_f is the fault shear strength, τ_d is the dynamic shear strength.

If D_c was small and/or the strength dropped, i.e., τ_f -τ_d was large, L_n became short. In the present study, D_c was assumed to be 0.03 m, based on typical seismic observations (Abercrombie and Rice 2005), τ_f -τ_d was taken as $0.1\sigma_n$, so the shear stress drop was 2.0 MPa (with an average σ_n of 20 MPa, ranging from 14 MPa to 34 MPa as shown in Fig. 6a). These assumptions resulted in L_n being 138 m. Based on the slip data in Table 4, we could consider the limitation of D_m as 90 m (Fig. 9).

Our simulation results enable the accurate prediction of coseismic slip distribution, which is crucial for identifying the area most susceptible to seismic events. By pinpointing these high-risk zones, mining operations can be planned to avoid or reinforce these areas, thereby minimizing the potential for significant seismic disturbances. Additionally, our method facilitates the redefinition of safe mining stop lines, particularly in deep mining operations where traditional guidelines may be inadequate (National Coal Mine Safety Administration 2000). By considering both shear and normal stress changes that cause fault slip to meet the nucleation length (L_n), which may further induce earthquakes, we estimate seismic magnitudes and nucleation sizes. This approach allows us to establish new stop lines that mitigate the risk of fault reactivation and coseismic slip.

Discussions

Stress drop

Stress drop, which is the difference in shear stress across a fault before and after an earthquake rupture, is directly associated with the elastic energy released as a consequence of an earthquake rupture (Sato 1972; Kanamori and Anderson 1975; Mayeda and Walter 1996). Fukuyama and Madariaga (1995) derived a relationship between slip and stress drop, which is consistent with the previous works, as a new boundary integral equation of dynamic tensile and shear cracks. They explicitly demonstrated that the final stress drop on the fault was equivalent for both static and dynamic problems.

As shown in Fig. 10a, under the condition of r_b = 2 and μ_s = 0.7, the mining-induced stress drop ranged from −6.1 MPa to 6.7 MPa in the case of D_m = 10 m, -1.0 MPa to 1.7 MPa in the case of D_m = 40 m, and −0.4 MPa to 0.8 MPa in the case of D_m = 90 m. The large slip zone caused a larger stress drop zone, and the large slip magnitude generated large values of the stress drop.

To validate the stress drop distribution calculated through Code_Aster, we compared it with that of DC3D (Okada 1992). DC3D provided us with a theoretical representation of fault slip and strain distribution around the fault formulated by Okada (1985) and Okada (1992). We used a subroutine package for DC3D (https://www.bosai.go.jp/e/dc3d.html) to calculate displacement and its space derivatives at any arbitrary point on the inside or surface of the elastic half-space medium due to a uniform slip on a finite rectangular fault.

Since the mining-induced fault slip was not uniform, we assumed a piecewise constant slip distribution divided at an interval of 10 m and computed the stress drop distribution by summing the stress change from these fault elements. In Fig. 10b and c, and 10d, the bars shown at the bottom indicated the approximated slip distribution and were used as input to DC3D. The stress drop distribution calculated by DC3D was shown as solid lines with open circles for three cases (D_m = 10 m, 50 m, and 90 m) under the condition of r_b = 2 and μ_s = 0.7. The mining-induced stress drop calculated by DC3D ranged from −7 MPa to 4.6 MPa for D_m = 10 m, -2.1 MPa to 2.1 MPa for D_m = 50 m, and −0.7 MPa to 1.0 MPa for D_m = 90 m. These results were consistent with the results by Code_Aster, shown as solid lines in Figs. 10b-d.

In Fig. 10a, we noticed a slight difference in stress distributions between Code_Aster and DC3D. A possible reason for this difference may come from the effect of mesh size in the model used in Code_Aster, especially from the contact interface mesh size on the fault. This was because

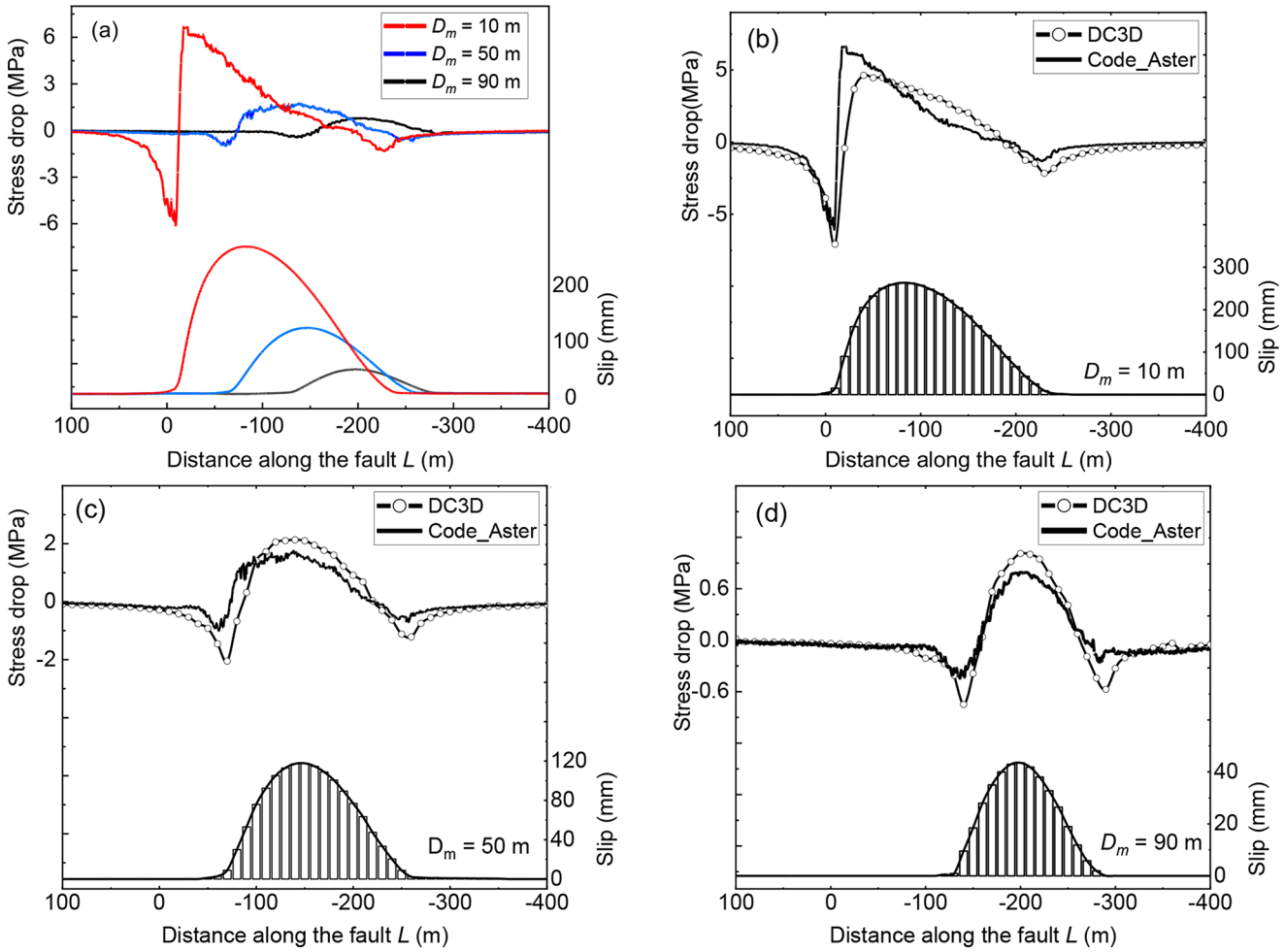

Fig. 10 Distribution of stress drop (top) and coseismic slip displacement (bottom) for different D_m under r_b = 2, μ_s=0.7, and φ=30°. **a** Stress drops and slip distributions for different D_m obtained from Code_Aster. Comparison of stress drop slip distributions between Code_Aster and DC3D for the case of **b** D_m = 10 m, **c** D_m = 50 m, and **d** D_m = 90 m. The rectangle at the bottom of the figure indicates the piecewise constant slip distribution used in DC3D, and the black curve is the coseismic slip obtained by the Code_Aster

when we used a coarse mesh model, the discrepancy in stress distribution increased. Actually, we constructed the mesh model that consists of 216,486 tetrahedron elements whose element size at the contact interface was about 0.5 m. This model was close to the limitation in Salome-Meca Ver. 2015.1 with the computer available at this moment. While we could not assert the perfect validity of the present Code_Aster computation, we believed that both results would converge if we decreased the element size of Code_Aster to infinitesimally small.

Application to the mining-induced earthquake in Yuejin coal mine

On August 11th, 2010, an earthquake with a M_L of 2.7 occurred at the No. 25,110 working face in the Yuejin coal mine, which was the reactivation of the reverse fault named F16 (Cai et al. 2015, 2021). This event was considered a mining-induced earthquake in our model, occurring at D_m equal to -80 m (Li et al. 2018). Considering actual conditions such as coal seam thickness, mining depth, fault dip angle, working face locations, background stress, and fault friction parameters (Table 1), we constructed a similar model as that of the Yuejin coal mine (Fig. 8c).

Our numerical simulation results predicted an earthquake magnitude range of $2.0 \leq M_w \leq 2.8$. This is not surprising, as the mining dimension is roughly equivalent to that of magnitude 2 earthquakes. In our simulation, an earthquake was induced when D_m reached 90 m, a value akin to D_m from the actual event. However, it should be reminded that our estimate includes a significant amount of uncertainty, especially in fault friction. Despite these uncertainties, our proposed procedure and simulation results can help estimate the coseismic slip distribution due to mining activities and provide crucial information for optimizing mining design and enhancing the safety of mining operations.

In contrast, local magnitude (M_L) is primarily used for field observations of small earthquakes. M_L is an empirical scale based on the observed maximum amplitudes of recorded seismographs. For small earthquakes ($M \sim 3$), M_L and moment magnitude (M_w) are generally consistent. Actually, several empirical relations are proposed. For example, $M_w = 0.81\ M_L + 0.61$ for California (Bakun and Lindh 1977) and $M_w = 0.64\ M_L + 0.84$ for Italy (Bindi et al. 2005). For more details, please refer to Table 6.11 in Havskov and Ottemoller (2010). The magnitude of the Yuejin coal mine event was M_L 2.7. Following the above conversion relations, M_L 2.7 corresponds to M_w 2.8 for California (Bakun and Lindh 1977) or M_w 2.6 for Italy (Bindi et al. 2005).

Fault reactivation: fault failure and coseismic slip

We considered fault reactivation in two aspects: fault failure and coseismic slip. By analyzing the fault stress ratio (k) in a reverse fault environment, we evaluated the sensitivity of various parameters to mining-induced fault instability. A mining-induced earthquake occurred on November 3, 2011, when mining reached near the F16 fault (Cai et al. 2015, 2021). Jiao et al. (2021) developed a refined 3-D numerical model to analyze stress evolution in the surrounding rock near the F16 fault during mining. They used in-situ stress data and geological information around the F16 fault. They observed a decrease in normal stress and an increase in shear stress on the upper fault plane when mining approaches the fault.

In this study, we further estimated the coseismic slip distribution resulting from mining, taking into account the fault friction properties as well as the stress field applied as the working face approached. We observed a significant sensitivity of k along the fault to the dip angle φ, particularly for small φ values, which was also illustrated in Jiao et al. (2021). Coal mining, in such cases, leads to a notable increase in k; thus, it increases the potential for induced earthquakes. By analyzing the fault stress ratio (k) with friction parameters in a reverse fault environment, we assessed the sensitivity of various parameters to mining-induced fault instability. Cai et al. (2021) developed a 3-D numerical model to analyze stress evolution in the surrounding rock near the F16 fault during mining, using in-situ stress data and geological information. They observed a high stress concentration around the coal pillar as mining approached the fault, which is also measured in the current study. However, a simple analysis of the stress state that did not account for the stress ratio and subsequent coseismic slip is not sufficient to capture the fault-induced coal bursts. In this study, we estimated the coseismic slip distribution resulting from mining by considering the fault friction properties and the stress field as the working face approached. Ultimately, earthquakes may be induced when the coseismic slip zone exceeds L_{n} (Uenishi and Rice 2003).

Zhang et al. (2022) reported the implementation of a pre-mining grouting technique as an idea to enhance the strength of the fault plane, ensuring safety during mining operations in the Yangcun coal mine. As shown in Figs. 9 and 11 of Zhang et al. (2022), on-site grouting significantly reduced fault slip displacement and ensured safe mining operations across the fault and, suppressed inducing earthquakes. Our computation results support their results and observations that the fault coseismic slip was reduced by increasing the fault frictional strength by grouting. In our computation, increasing the friction coefficient from 0.5 to 0.8 results in a substantial reduction in coseismic slip from 280 m to 90 m (Fig. 7).

Limitations

The main assumptions of this study were the background stress and friction properties of the fault. Regarding the background stress field, we do not include the heterogeneity of the material, which might alter the stress field. In the practical application of this approach, the material structure should be properly included in the model, which could be feasible in most cases. The background stress ratio r_b also affects the predicted slip distribution on the fault. The parameter r_b does not need to remain constant along the depth; it may vary. Our methodology is capable of accommodating this heterogeneity, ensuring accurate modeling and analysis.

Regarding the friction property on the fault, we assumed zero cohesion on the fault. This assumption was sometimes applied to ore mines and gas mines, where the mining-induced fault reactivation process was considered (e.g., Sainoki and Mitri 2014, 2015; Buijze et al. 2019). Some studies pointed out that cohesion also affects the mining-induced fault stress ratio and coseismic slip (Bizzarri 2010); we should carefully input the cohesion into the simulation. The friction coefficient used in our simulations was based on Byerlee's law (Byerlee 1978) and data from studies on induced earthquakes (Cai et al. 2021). Materials with plate-like structures, such as graphite and talc, exhibited lower friction compared to rocks and minerals with bulk structures. These minerals, often products of hydrothermal alteration, were commonly found in fault gouges and could significantly influence fault strength (Nguyen et al. 2016; Garofalo et al. 2023). Therefore, investigation of the friction properties of these minerals was deemed a valuable area for future research. In addition, fault geometry is crucial because this affects the global friction property as well as the stress ratio on the fault (Hok et al. 2011).

The estimation of the nucleation size (L_n) was based on the assumed breakdown shear strength drop (τ_f -τ_d) and critical

slip distance (D_c). L_n was estimated by friction parameters but these parameters are quite difficult to measure in the field but can be obtained by laboratory experiments. We now examine the uncertainty in the friction parameters on L_n. If D_c is increased by 20% from our assumed value, while other conditions remain the same, L_n will increase to 178 m, requiring the terminal mining line to be at least 50 m away from the fault. Similarly, based on Eq. (10), we can evaluate the uncertainty in τ_f -τ_d on the nucleation length. Hence, it should be emphasized that the parameters, D_c and τ_d need to be carefully estimated for practical applications. Once we obtain these values reliably, we can evaluate the nucleation length following Uenishi and Rice (2003).

Conclusions

We conducted a numerical investigation to explore fault failure and coseismic slip phenomena under the conditions of deep coal mining, considering multiple variables including φ (fault dip angle), r_b (background stress ratio), D_m (mining distance), and μ_s (fault frictional strength). Our numerical modeling demonstrated that fault reactivations occur not only due to shear stress concentration but also as a result of a decrease in normal stress. Therefore, we proposed that monitoring the k value will serve as the indication for mining-induced fault reactivation. Moreover, the value of k along the fault is found to be highly sensitive to the φ parameter. When φ is small, coal mining will substantially increase the k value on the fault, elevating the potential for induced earthquakes.

We found that hanging wall mining induces fault instability beneath the mining level, whereas footwall mining generates slip above the mining level. And footwall mining yields greater instability under similar conditions. Both μ_s and D_m are critical in determining coseismic slip and Δk. To accurately assess the terminal mining line without inducing earthquakes, we conducted quantitative evaluations of in-situ monitoring values for parameters such as stress field, fault geometry, and fault friction. Nevertheless, further investigations are needed to assess the size of the nucleation zone in order to precisely quantify the terminal mining line.

Acknowledgements Comments by two anonymous reviewers were helpful. Critical reading of the manuscript by Dr. Shibo Xu was quite valuable.

Author contributions The study conception and design were carried out by Eiichi Fukuyama. Numerical experiments were conducted by Yatao Li. The first draft of the manuscript was prepared by Yatao Li. All authors read, revised, and approved the manuscript.

Funding This research was supported by JSPS KAKENHI Grant Number JP22H01321, JP23K22592. Yatao Li was supported by Japanese Government (MEXT) Scholarship.

Data availability All data generated or analyzed during this study are available from the corresponding author upon request.

Declarations

Competing interests The authors declare that there is no conflict of interest regarding the publication of this paper.

References

Abercrombie RE, Rice JR (2005) Can observations of earthquake scaling constrain slip weakening? Geophys J Int 162(2):406–424. https://doi.org/10.1111/j.1365-246X.2005.02579.x

Aki K (1967) Scaling law of seismic spectrum. J Geophys Res 72(4):1217–1231. https://doi.org/10.1029/JZ072i004p01217

Aki K, Richard PG (2009) Quantitative seismology, 2nd edn. University Science Books, p 700

Andrews DJ (1976) Rupture velocity of plane strain shear cracks. J Geophys Res 81(32):5679–5687. https://doi.org/10.1029/JB081i032p05679

Bakun WH, Lindh AG (1977) Local magnitudes, seismic moments, and coda durations for earthquakes near Oroville, california. Bull Seismol Soc Am 67(3):615–629. https://doi.org/10.1785/BSSA0670030615

Balsamo F, Storti F, Salvini F, Silva A, Lima C (2010) Structural and petrophysical evolution of extensional fault zones in low-porosity, poorly lithified sandstones of the Barreiras formation, NE Brazil. J Struct Geol 32:1806–1826. https://doi.org/10.1016/j.jsg.2009.10.010

Bindi ML, Biancofiore G, Meacci L, Bellissima G, Nardi S, Pieri M, Vistoli F, Boggi U, Sansevero A, Mosca F (2005) Early morbidity after pancreas transplantation. Transpl Int 18(12):1356–1360. https://doi.org/10.1111/j.1432-2277.2005.00222.x

Bizzarri A (2010) How to promote earthquake ruptures; different nucleation strategies in a dynamic model with slip-weakening friction. Bull Seismol Soc Am 100(3):923–940. https://doi.org/10.1785/0120090179

Buijze L, van den Bogert, Peter AJ, Wassing BBT, Orlic B (2019) Nucleation and arrest of dynamic rupture induced by reservoir depletion. J Geophys Res Solid Earth 24(4):3620–3645. https://doi.org/10.1029/2018JB016941

Byerlee J (1978) Friction of rocks. Pure Appl Geophys 116(4):615–626. https://doi.org/10.1007/bf00876528

Cai W, Dou L, Li Z, He J, He H, Ding Y (2015) Mechanical initiation and propagation mechanism of a thrust fault; a case study of the Yima section of the Xiashi-Yima thrust (north side of the eastern Qinling orogen, China). Rock Mech Rock Eng 48(5):1927–1945. https://doi.org/10.1007/s00603-014-0666-x

Cai W, Dou L, Si G, Hu Y (2021) Fault-induced coal burst mechanism under mining-induced static and dynamic stresses. Eng (Beijing China) 7(5):687–700. https://doi.org/10.1016/j.eng.2020.03.017

Cao Y, He D, Glick DC (2001) Coal and gas outbursts in footwalls of reverse faults. Int J Coal Geol 48:47–63. https://doi.org/10.1016/S0166-5162(01)00037-4

Chen L, Shen B, Dlamini B (2018) Effect of faulting on coal burst - A numerical modeling study. Int J Min Sci Technol 28(5):739–743. https://doi.org/10.1016/j.ijmst.2018.07.010

Foulger GR, Wilson MP, Gluyas JG, Julian BR, Davies RJ (2018) Global review of human-induced earthquakes. Earth Sci Rev 178:438–514. https://doi.org/10.1016/j.earscirev.2017.07.008

Fukuyama E, Madariaga R (1995) Integral equation method for plane crack with arbitrary shape in 3D elastic medium. Bull Seismol Soc Am 85(2):614–628. https://doi.org/10.1785/BSSA0850020614

Garofalo PS, Maffei J, Papeschi S, Dellisanti F, Neff C, Schwarz G, Schmidt PK, Günther D (2023) Fluid-rock interaction, skarn genesis, and hydrothermal alteration within an upper crustal fault zone (island of Elba, Italy). Ore Geol Rev 154:105348. https://doi.org/10.1016/j.oregeorev.2023.105348

Geller RJ (1976) Scaling relations for earthquake source parameters and magnitudes. Bull Seismol Soc Am 66(5):1501–1523. https://doi.org/10.1785/BSSA0660051501

Hanks TC, Kanamori H (1979) A moment magnitude scale. J Geophys Res 84:2348–2350. https://doi.org/10.1029/JB084iB05p02348

Havskov J, Ottemoller L (2010) Routine data processing in earthquake seismology: With sample data, exercises and software. Springer Science + Business Media. https://doi.org/10.1007/978-90-481-8697-6

Hok S, Fukuyama E, Hashimoto C (2011) Dynamic rupture scenarios of anticipated Nankai-Tonankai earthquakes, southwest Japan. J Geophys Res 116:B12319. https://doi.org/10.1029/2011JB008492

Jaeger JC, Cook NGW, Zimmerman RW (2007) Fundamentals of Rock mechanics, 4th edn. Blackwell Pub, p 475

Jiao Z, Wang L, Zhang M, Wang J (2021) Numerical simulation of mining-induced stress evolution and fault slip behavior in deep mining. Adv Mater Sci Eng 2021:1–14. https://doi.org/10.1155/2021/8276408

Kanamori H, Anderson DL (1975) Amplitude of the earth's free oscillations and long-period characteristics of the earthquake source. J Geophys Res 80(8):1075–1078. https://doi.org/10.1029/JB080i008p01075

Kang H, Gao F, Xu G, Ren H (2023) Mechanical behaviors of coal measures and ground control technologies for China's deep coal mines – A review. J Rock Mech Geotech Eng 15(1):37–65. https://doi.org/10.1016/j.jrmge.2022.11.004

Karacan CO, Ulery JP, Goodman GVR (2008) A numerical evaluation on the effects of impermeable faults on degasification efficiency and methane emissions during underground coal mining. Int J Coal Geol 75(4):195–203. https://doi.org/10.1016/j.coal.2008.06.006

Kostrov BV, Das S (1988) Principles of earthquake source mechanics, 286pp edn. Cambridge University Press

Li T, Cai MF, Cai M (2007) A review of mining-induced seismicity in China. Int J Rock Mech Min Sci 44(8):1149–1171. https://doi.org/10.1016/j.ijrmms.2007.06.002

Li Z, Dou L, Cai W, Wang G, He J, Gong S, Ding Y (2014) Investigation and analysis of the rock burst mechanism induced within fault-pillars. Int J Rock Mech Min Sci 70:192–200. https://doi.org/10.1016/j.ijrmms.2014.03.014

Li P, Ren F, Wang H, Qian J, IOP (2018) An overview of fault rockburst in coal mines. 2018 First Int Conf Environ Prev Pollution Control Technol (Eppct 2018) 1995(52039). https://doi.org/10.1088/1755-1315/199/5/052039

Lyu P, Lu J, Wang E, Chen X (2021) The mechanical criterion of activation and instability of normal fault induced by the movement of key stratum and its disaster-causing mechanism of rockburst in the hanging wall mining. Adv Civil Eng 2021:1–11. https://doi.org/10.1155/2021/6618957

Mark C (2016) Coal bursts in the deep longwall mines of the United States. Int J Coal Sci Technol 3(1):1–9. https://doi.org/10.1007/s40789-016-0102-9

Mayeda K, Walter WR (1996) Moment, energy, stress drop, and source spectra of western United States earthquakes from regional coda envelopes. J Geophys Res Solid Earth 101(B5):11195–11208. https://doi.org/10.1029/96JB00112

National Coal Mine Safety Administration (2000) State coal industry bureau building, water, railway and main shaft coal pillar of coal mining and coal mining regulations. Coal Industry Publishing House, Beijing, pp 236–238

Nguyen GD, Nguyen CT, Bui HH, Nguyen VP (2016) Constitutive modeling of compaction localization in porous sandstones. Int J Rock Mech Min Sci 83:57–72. https://doi.org/10.1016/j.ijrmms.2015.12.018

Okada Y (1985) Surface deformation due to shear and tensile faults in a half-space. Bull Seismol Soc Am 75(4):1135–1154. https://doi.org/10.1785/BSSA0750041135

Okada Y (1992) Internal deformation due to shear and tensile faults in a half-space. Bull Seismol Soc Am 82(2):1018–1040. https://doi.org/10.1785/BSSA0820021018

Ranjith PG, Zhao J, Ju M, De Silva RVS, Rathnaweera TD, Bandara AKMS (2017) Opportunities and challenges in deep mining: a brief review. Engineering 3(4):546–551. https://doi.org/10.1016/J.ENG.2017.04.024

Sainoki A, Mitri HS (2014) Dynamic behaviour of mining-induced fault slip. Int J Rock Mech Min Sci 66:19–29. https://doi.org/10.1016/j.ijrmms.2013.12.003

Sainoki A, Mitri HS (2015) Effect of slip-weakening distance on selected seismic source parameters of mining-induced fault-slip. Int J Rock Mech Min Sci 73:115–122. https://doi.org/10.1016/j.ijrmms.2014.09.019

Sato R (1972) Stress drop for a finite fault. J Phys Earth 20(4):397–407. https://doi.org/10.4294/jpe1952.20.397

Scholz CH (2019) The mechanics of earthquakes and faulting, 493pp edn. Cambridge University Press

Shan R, Liu D, Wang H, Tong X, Li Z, Zhao Y (2023) Study of the fracture instability and fault slip risk of overlying strata during mining near faults. Bull Eng Geol Environ 82(3). https://doi.org/10.1007/s10064-023-03112-8

Song W, Liang Z (2021) Theoretical and numerical investigations on mining-induced fault activation and groundwater outburst of coal seam floor. Bull Eng Geol Environ 80(7):5757–5768. https://doi.org/10.1007/s10064-021-02245-y

Uenishi K, Rice JR (2003) Universal nucleation length for slip-weakening rupture instability under nonuniform fault loading. J Geophys Res 108(B1):2042. https://doi.org/10.1029/2001JB001681

Verdon JP, Kendall JM, Butcher A, Luckett R, Baptie BJ (2018) Seismicity-induced by longwall coal mining at the Thoresby colliery, Nottinghamshire, U. K. Geophys J Int 212(2):942–954. https://doi.org/10.1093/gji/ggx465

Wang H, Shi R, Song J, Tian Z, Deng D, Jiang Y (2021) Mechanical model for the calculation of stress distribution on fault surface during the underground coal seam mining. Int J Rock Mech Min Sci 144:104765. https://doi.org/10.1016/j.ijrmms.2021.104765

Wei C, Zhang C, Canbulat I, Anye C, Linming D (2018) Evaluation of current coal burst control techniques and development of a coal burst management framework. Tunn Undergr Space Tech 81:129–143. https://doi.org/10.1016/j.tust.2018.07.008

Wei C, Zhang C, Canbulat I (2020) Numerical analysis of fault-slip behavior in longwall mining using linear slip weakening law. Tunn Undergr Space Tech 104:103541. https://doi.org/10.1016/j.tust.2020.103541

Wells DL (2013) Updated empirical relationships among magnitude, rupture area, rupture length, and surface displacement. Seismol Res Lett 84(2):309

Wells DL, Coppersmith KJ (1994) New empirical relationships among magnitude, rupture length, rupture width, rupture area, and surface displacement. Bull Seismol Soc Am 84(4):974–1002. https://doi.org/10.1785/bssa0840040974

Wu Q, Wu Q, Yuan A, Wu Y (2021) Analysis of mining effect and fault stability under the influence of normal faults. Geotech Geol Eng 39(1):49–63. https://doi.org/10.1007/s10706-020-01400-8

Zhang W, Lei Y, Shao J, Wu X, Li S, Ma C (2022) Simulation of the activation of mining faults and grouting reinforcement under

thick loose layer and thin bedrock. Sci Rep 12(1):17049–17049. https://doi.org/10.1038/s41598-022-21654-x

Zhang N, Zhang Z, Shan R, Qi Q, Zhao S, Sun Z, Guo Y (2023) An experimental study of fault slips under unloading condition in coal mines. Bull Eng Geol Environ 82(4). https://doi.org/10.1007/s10064-023-03125-3

Zhou K, Dou L, Li X, Song S, Cao J, Bai J, Ma X (2022) Coal burst and mining-induced stress evolution in a deep isolated main entry area - a case study. Eng Fail Analy 137:106289. https://doi.org/10.1016/j.engfailanal.2022.106289

Zhu Q, Zhao X, Westman E (2021) Review of the evolution of mining-induced stress and the failure characteristics of surrounding rock based on microseismic tomography. Shock Vib 2021:1–19. https://doi.org/10.1155/2021/2154857